Available online at www.sciencedirect.com

jmr&t Journal of Materials Research and Technology

journal homepage: www.elsevier.com/locate/jmrt

Original Article

Development of a complex multicomponent microstructure on commercial carbon-silicon grade steel by governing the phase transformation mechanisms to design novel quenching and partitioning processing

Felipe M. Carvalho [a], *Dany Centeno* [b], *Gustavo Tressia* [c], *Julian A. Avila* [d,e], *Fabiano E.M. Cezario* [f], *Andrés Márquez-Rossy* [g], *Edwan A. Ariza* [b,h,*], *Mohammad Masoumi* [f,**]

[a] *Metallurgical Processes Laboratory, Institute for Technological Research, Av. Prof. Almeida Prado, 532 São Paulo, Brazil*

[b] *Metallurgical and Materials Engineering Department, University of São Paulo, Av. Prof. Mello Moraes, 2463, São Paulo, Brazil*

[c] *Instituto Tecnológico Vale, Av. Juscelino Kubitschek 3, Bauxita, Ouro Preto, MG, 35400-000, Brazil*

[d] *Department of Strength of Materials and Structural Engineering, Barcelona School of Engineering (ETSEIB), Universitat Politècnica de Catalunya, Avda. Diagonal 647, 08028 Barcelona, Spain*

[e] *São Paulo State University (UNESP), São João da Boa Vista, SP, 13876-750, Brazil*

[f] *Center of Engineering, Modelling and Applied Social Sciences, Federal University of ABC, UFABC, Santo Andre, Sao Paulo, Brazil*

[g] *Materials Science & Technology Division, Oak Ridge National Laboratory, Oak Ridge, TN, USA*

[h] *Escuela de Tecnología Mecánica, Universidad Tecnológica de Pereira, Carrera 27 #10-02 Alamos, Pereira, 660003, Colombia*

ARTICLE INFO

Article history:
Received 8 March 2022
Accepted 12 April 2022
Available online 28 April 2022

Keywords:
Nanoparticles
Lattice distortion
Boundaries
Kernel average misorientation
Crystal orientation

ABSTRACT

The constant demand for increasing the strength without ductility loss and production cost encourages industrial and academic societies to propose novel heat treatment processing of commercial steel grades. To improve the mechanical properties of commercial spring steel, a novel quenching and partitioning (Q&P) processing was designed to deliver a complex and desirable nanostructured multicomponent microstructure by controlling the carbon partitioning kinetics. Furthermore, the partitioning of excessive carbon from saturated martensite into untransformed austenite enhances the formation of transition carbides during tempering between 130 and 280 °C. Electron microscopy confirmed a complex multicomponent structure containing BCC tempered lath combined with retained austenite and nanocarbides particles within the tempered laths. Such multicomponent lath-type structure obtained by designed Q&P heat treatment on commercial carbon-

* Corresponding author.
** Corresponding author.
E-mail addresses: andersonariza@usp.br (E.A. Ariza), mohammad.m@ufabc.edu.br (M. Masoumi).

https://doi.org/10.1016/j.jmrt.2022.04.066

silicon spring steel revealed localized mechanical resistance varying from 4.92 GPa for the QP-220-375-400 to 8.22 GPa for the QP-220-325-400 samples determined by nanoindentation test. Moreover, the tensile test showed high ultimate tensile strength and a yield strength up to 1400 MPa and 975 MPa, respectively, in the QP-220-375-400 sample due to a set of complex multicomponent lath-type refined structures designed by Q&P coupled with bainitic transformation, with good strain to fracture (~0.12%).

1. Introduction

The development of new advanced high strength steels (tensile strength above ~600 MPa) and good formability is the main interest in different industries to reduce body and fuel consumption without decreasing safety. Lean automotive industries proposed alloys to generate multiphase microstructures with a high density of interfaces, to avoid using expensive alloying elements such as nickel to reduce steelmaking production. In this regard, tailoring multiphase systems, i.e., ferrite, bainite, martensite, and retained austenite in steels, and their balance of phase stability in microstructure, provides a superior strength-ductility response. Moreover, many phases and high angle boundaries act as dislocation sources, dislocation movement barriers, and even enhance stress/strain concentrations, resulting in superior strength with acceptable damage tolerance.

Recently, commercial medium-carbon silicon steels (Fe-0.55C-1.5Si-0.8Mn-0.8Cr and Fe-0.6C-2.0Si-0.9Mn (wt.%)) are attracted especial attention due to their excellent ultimate tensile strength (min 660 MPa) and elongation (min 20%). Also, a remarkable amount of Si content in these steels is considered a promising candidate material for the third generation of advanced high strength steels (AHSSs). The quenching and partitioning (Q&P) process, according to Speer in 2003 [1], proposed a non-equilibrium heat treatment technique for achieving ultra-high-strength with good ductility due to set fine-lath martensite and carbon enriched retained austenite. In two-step Q&P, first, austenitizing or intercritical annealing is employed to produce a certain fraction of austenite and ferrite, followed by quenching to a temperature between the martensite start and finish temperatures to form known fraction martensite products. Then, isothermal holding at higher temperatures than quench temperature permits partitioning the excess carbon content into untransformed austenite. Microstructure evolution, austenite/martensite interface migration, and martensite tempering reactions occur during Q&P processing [1–4]. The transformation-induced plasticity (TRIP) effect can significantly improve mechanical, fatigue, and wear behavior depending on the stability, morphology, and size of retained austenite.

The mechanism of carbon partitioning during partitioning from saturated martensite into untransformed austenite has been debated since the introduction of Q&P processing. The austenite morphology and characteristics of the martensite, such as the carbon supersaturation (i.e., tetragonality), also influence carbon diffusion. On the other hand, the quantity and stability of the retained austenite in TRIP steels also play essential roles in determining their mechanical properties. The stability of the retained austenite can be affected by its chemical composition, morphology, and interface with adjacent martensite. Recently, Xiong et al. [5] reported that martensitic transformation occurs in high carbon blocky retained austenite, while low carbon film-like retained austenite is stable at strains up to 12%. This behavior may be due to the higher yield strength of lath martensite surrounded by film-like retained austenite, while blocky austenite was surrounded by softer proeutectoid ferrite. In addition, alloying elements influence cementite formation; for instance, the solubility of silicon is incredibly low. Thereby, a certain amount of silicon (at least 1.5 wt.%) inhibits the formation of carbides.

On the other hand, bainite formation during Q&P affects the austenite enrichment [4,6–9]. Bigg et al. [2,10] investigated the austenite and martensite/ferrite lattice parameter changes by in situ neutron diffraction. They reported clear evidence of carbon partitioning from the supersaturated martensite to the retained austenite. Clarke et al. [2,11] investigated the mechanisms for austenite carbon enrichment during partitioning by APT and transmission electron microscopy (TEM). They confirmed that carbon partitioning from martensite provides a more satisfactory explanation, although bainite formation during partitioning cannot be wholly excluded. Finally, Ariza et al. [4,6,12,13] proposed that the crystallographic orientations and interface boundaries between austenite and ferrite/martensite phase could influence the carbon partitioning mechanism.

This paper studied the tempering behavior of a commercial medium carbon-silicon steel followed by tempering through dilatometry to design a novel Q&P path. In addition, microstructure evolution during proposed Q&P processing was explored using scanning electron microscopy (SEM) and Electron Backscattered Diffraction (EBSD) technique to investigate the crystallographic data and microstructure simultaneously to validate our predictions about achieving superior mechanical resistance by tailoring the microstructural features.

2. Experimental method

The chemical composition of the steel examined in this investigation is listed in Table 1. First, the ingot was prepared

Table 1 – Chemical compositions of the examined alloy (wt.%).

C	Si	Mn	Cr
0.53	1.54	0.86	0.88

by vacuum induction melting. Next, 19 mm slabs were machined from the ingot to conduct the hot rolling step. Finally, the slab was reheated in an induction furnace for 5 min at 1250 °C and then hot-rolled into 5 mm thick plate samples in 6 steps, each with rolling reductions in 22%. The microstructure of the as-received studied samples is shown in Fig. 1.

Dilatometry was used to find the temperatures associated with critical transformation temperatures such as start (Ac_1) and finish (Ac_3) austenitizing transformation, martensite starting (Ms) during heating, and rapid quenching rate at 20 °C/s and 50 °C/s. Fig. 2 shows proposed Q&P processing followed by bainitic transformation after a detailed study of the phase transformation mechanism. Proposed heat treatments were conducted on cylindrical specimens (4 mm diameter with 10 mm length) in high precision Bahr DIL 805 A/D dilatometer with fused silica rod as a reference and pure Ar gas for quenching medium. Type S Thermocouple (Platinum Rhodium - 10%/Platinum) was used for temperature measurement. Finally, the dilatation curve during heat treatment was carefully analyzed to reveal transformation kinetics. The steels are hereafter referred to as QP-220-325-400 and QP-220-375-400 due to the Quench&Partitioning-tempering temperature-first partitioning step-second partitioning step, respectively.

A detailed microstructural investigation was carried out using a scanning electron microscope (JSM-6010LA, JEOL). The metallographic samples preparation was conducted according to the standard procedures, including mounting, mechanical grinding, polishing, and etching with 2% Nital. EBSD measurements were done on an FEI-Inspect F50 SEM equipped with a field emission gun (FEG) and EBSD detector. Before the EBSD measurements, the samples were prepared according to the standard preparation and polished with 50 nm colloidal silica slurry for 3 h. All analyses were carried out with an accelerating voltage of 20 kV, a spot size of 5, a working distance of about 12 mm, and a step size of 20 nm with hexagonal scan grid mode. The EBSD and orientation data were analyzed using TSL OIM data analysis 7 and ATEX [3,14].

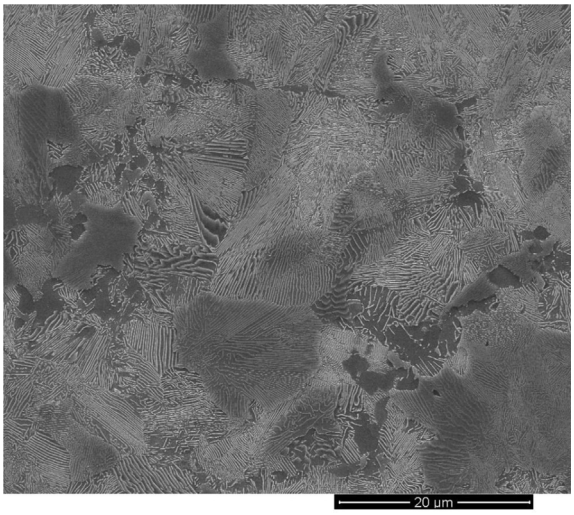

Fig. 1 – Commercial AISI 9254 steel grade microstructure of as-received condition.

To distinguish the mechanical performances of individual phases in the multiphase thermomechanical treated steels, nanoindentation was conducted on Triboindenter TI 950 (Hysitron Inc.) in load control testing mode. An array of 10 × 10 indentations was performed by applying a force of 3 mN using a Berkovich type indenter. The indenter tip was previously calibrated using a standard specimen of fused quartz to correlate the contact area with the penetration depth. The drift rate was restrained below 0.2 nm/s. Analyses of the hardness values were conducted using the method outlined by Oliver et al. [15]. Spacing between indents was 6 µm in both vertical and horizontal directions. All samples were tested at room temperature after metallographic samples preparation using a Buehler AutoMet 300 Pro and posterior ion-milling with a Hitachi ArBlade5000 at 6kV/1,5 kV (Acc V/Dis V) for 15 min. Additionally, subsize specimens were machined from the treated samples by a wire cut erosion discharge machine. Engineering stress-strain data was obtained from the average of three tensile samples at a strain rate of 2×10^{-3} s^{-1}.

3. Results and discussion

Fig. 3a represents the dilatation response with 5 °C/s and 50 °C/s heating and cooling rates, respectively, indicating phase transformation behavior. A gradual and linear volumetric expansion is observed up to 780 °C (Ac_1). At the inflection point (loss of the linearity), the body-centered cubic (BCC) ferrite matrix starts to transform to face-centered cubic (FCC) austenite; the transformation takes place until the curve resumes linear behavior. BCC structure contains two atoms per lattice, while the more compact FCC lattice has four atoms per lattice [16,17]. Therefore, a gradual contraction occurs until 820 °C (Ac_3), indicating a complete austenitization. After a while, the sample was rapidly quenched to form a body-centered tetragonal (BCT) martensite phase accompanied by significant volumetric expansion at ~ 300 °C (M_s).

Although Koistinen and Marburger's (K-M) model based on displacive transformation was proposed to describe the kinetics of martensite transformation, the complexity of

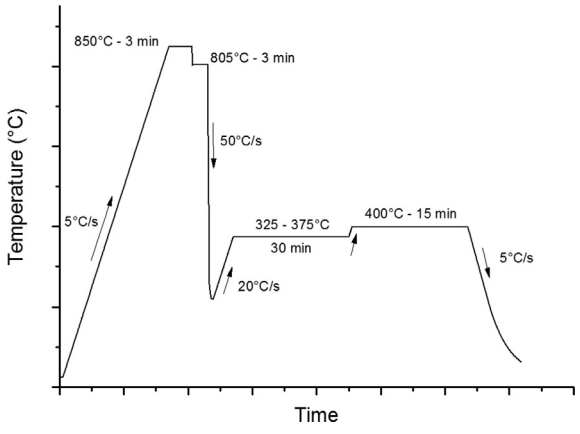

Fig. 2 – Schematic representation of proposed Q&P processing followed by bainitic transformation at QP-220-325-400 and QP-220-375-400 specimens.

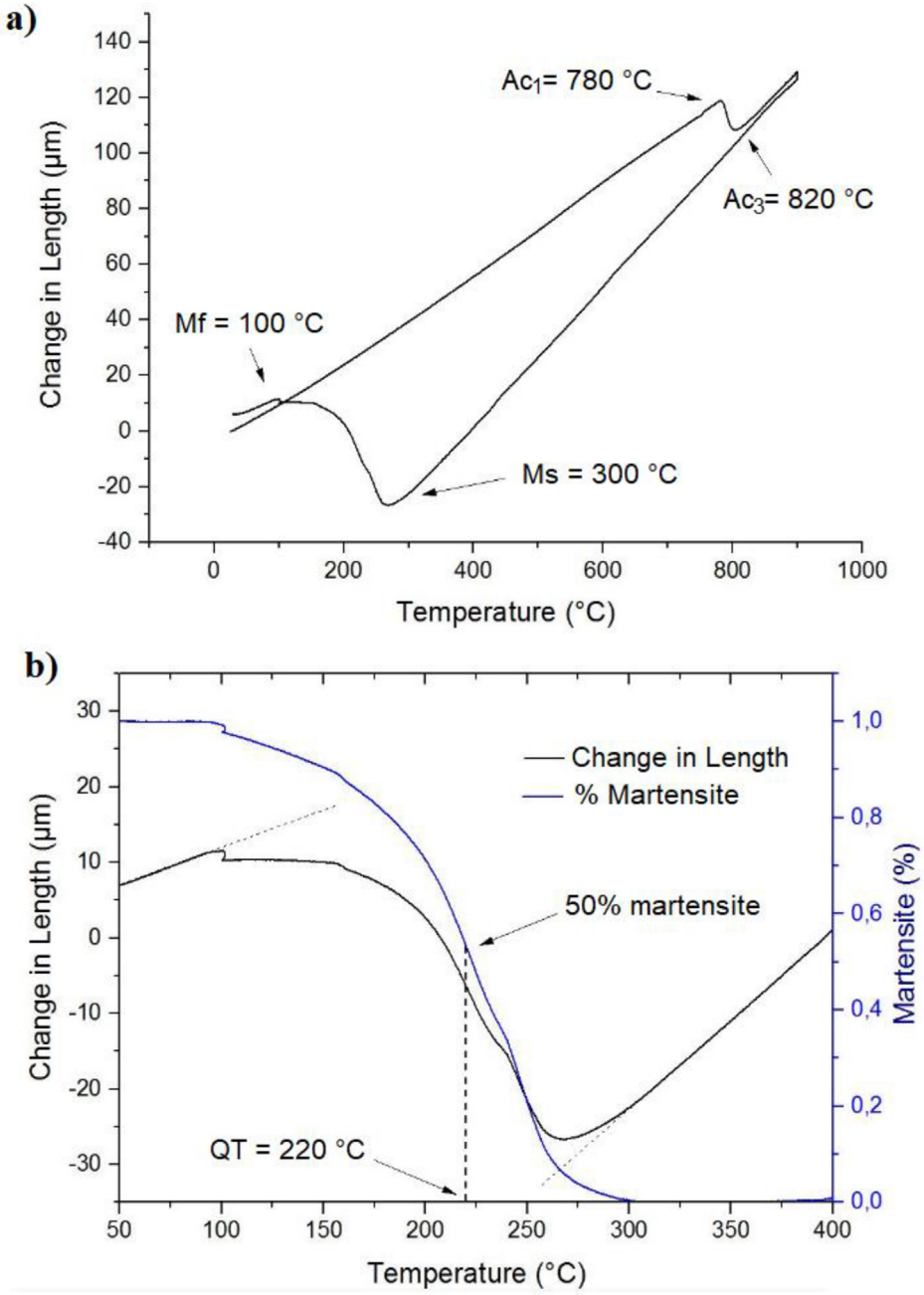

Fig. 3 – (a) Dilatation response during heating and cooling cycles, (b) experimental data results of kinetics of the martensite transformation during rapid quenching rate at 50 °C/s.

chemical composition in the austenite phase can induce some uncertainty [18]. Therefore, experimental data were analyzed to estimate the proper quenching temperature for tailoring a multicomponent microstructure. For this, the formation of martensite volumetric fraction was obtained from the lever rule associated with the dilatation data, as depicted in Fig. 3b. The martensite start and finish were evaluated at 300 °C and 100 °C, respectively. Displacive martensitic transformation, an extreme amount of α'/γ interfaces coupled with noticeable volumetric expansion and shear strain were formed due to the equivalence of Gibbs's free energy, storing energy in the system with metallurgical and crystallographic defects [12]. The martensite laths first would be formed mainly at grain boundaries and grown into the untransformed austenite grain. Subsequently, induced plastic deformation is gradually concentrated by increasing the martensite transformation and the resistance of untransformed austenite against martensite lath growth. This localized stress/strain concentration accompanied by heterogeneous carbon distribution in austenite promotes the formation of plate martensite. Peng et al. [19,20] reported two-stage martensite transformation under quenching: i) low carbon content austenite partially transformed into martensite at a higher temperature, then ii) more stable austenite regions with higher carbon content

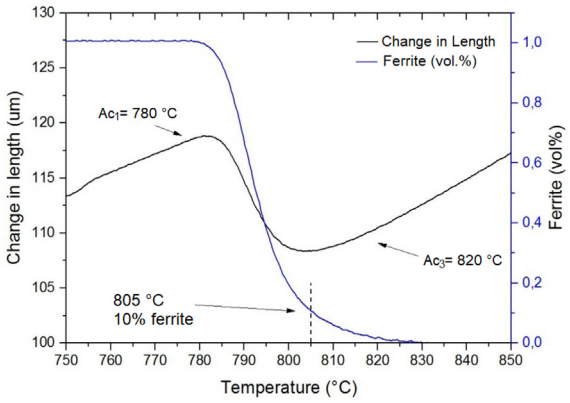

Fig. 4 – Lever rule of ferrite fraction as a function of austenitizing temperature.

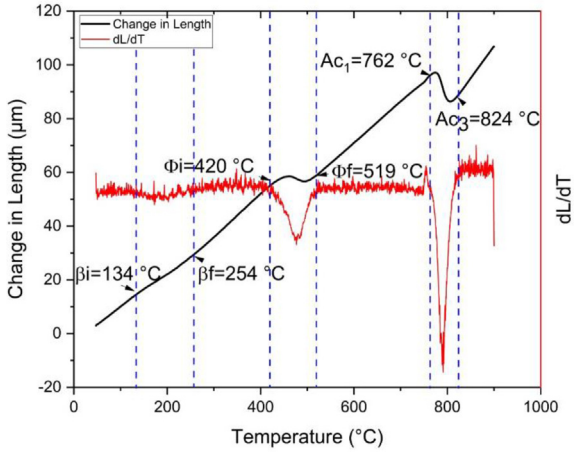

Fig. 5 – Dilatation behavior as a function of the temperature change of quenched specimen (βi, βf, ϕi, and ϕf representing bainite start, finish, and carbide start and finish temperatures).

remained unchanged surrounded by nanoscale martensite laths (or BCC laths). Hence, the formation of martensite blocks is accompanied by higher internal energy. The quenching temperature at 220 °C was determined to i) produce approximately 58% of austenite transformed into lath martensite and ii) avoid the formation of microcracks and high stress/strain concentration field due to partial martensitic transformation. Moreover, the mentioned high carbon content austenite regions could play a significant role in bainitic transformation during the partitioning stage and be highly important to the final microstructure.

As the M_s temperature was determined, thermal cycles were proposed to induce the formation of 10% of ferrite by an intercritical heat treatment between A_{C1} and A_{C3}. Using the lever rule (Fig. 4), the intercritical treatment was applied at 805 °C to produce a 10% ferrite and 90% austenite microstructure. Thus, the remaining austenite is available to transform through a quenching temperature between Ms and Mf partially. To partially quench the remaining austenite and transform 58% of this remaining austenite, the lever rule in the quenching dilatometry curve suggests a quenching temperature of 220 °C, as observed in Fig. 3b. At the quenching temperature, the microstructure was expected to contain the dispersion of carbide particles in a ferritic-martensitic structure. After quenching, the sample was submitted to the partition step to induce the stabilization of the remaining austenite. The partition temperatures used were 325 °C and 375 °C for 30 min. After partitioning, a tempering treatment at 400 °C for 15 min was proposed.

To study the influence of tempering temperature on body-centered cubic (BCT) martensitic microstructure, medium carbon-silicon commercial spring steels were austenitized entirely, followed by cooling water. The dilatation (percent length change) as a function of the temperature change of specimens was plotted in Fig. 5. In the range of 134 and 254 °C, a relatively small dilation change could be associated with the precipitation of transition carbide (probable ε-carbide $Fe_{2.4}C$ or η-carbide Fe_2C) [19,21]. The transition carbides were completely dissolved above 400 °C and replacement with stable cementite carbides in higher temperatures, confirmed by the dilatation results. A considerable contraction between 420 and 519 °C can be related to the decomposition of retained austenite in the ferritic bainite and carbides. Then, cementite precipitation and growth occurred entirely. A gradual martensite lattice relaxation can be observed by increasing the tempering temperature to convert BCT martensite into fine BCC acicular ferrite [2,10,13]. Tempering at higher temperatures (~550 °C) enhances the carbon rejection from martensite to form fine interleave carbides (~2 μm) dispersed in the ultrafine acicular ferrite (BCC martensite) [22]. Subsequently, carbon-enriched tetragonal martensite lost its tetragonality entirely and transformed into a mixture of the ultrafine acicular ferrite (laths, depleted in carbon) with nano-sized interleave carbides. Finally, austenitization during

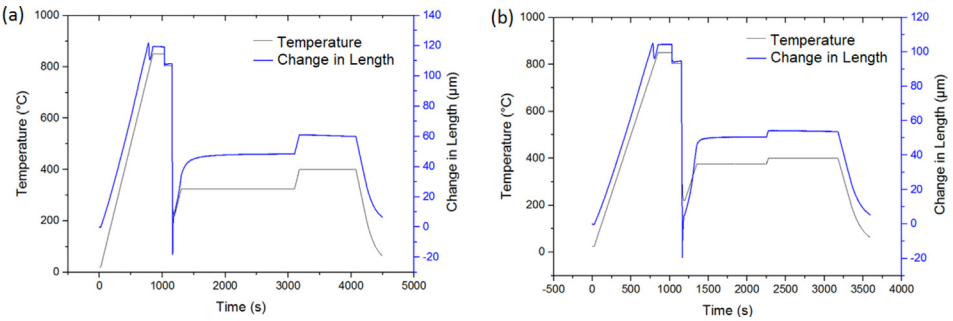

Fig. 6 – Experimental Dilatometry data of (a) QP-220-325-400 and (b) QP-220-375-400 specimens.

heating started at about 780 °C and ended at about 820 °C as A_{c1} and A_{c3}.

Dilatation behavior showed the formation of stable cementite carbide at 420 °C; thereby experimental partitioning step was determined, ranging from 325 °C to 375 °C for the first step and 400 °C in the subsequent partitioning stage, Fig. 6. Different lower bainitic structures would be formed under the first partitioning stage. Then, the bainitic transformation rate increased during the second partitioning step at 400 °C, without decomposition of retained austenite and formation of cementite particles.

Fig. 7 shows the different dilation variations due to the distinct phase transformations during the proposed novel heat treatments. First, the eutectoid phase transformation occurred during heating to 900 °C. Some transformations are evident: the start and end of austenitization (Ac_1 and Ac_3) and the martensitic transformation expansion in quenching (M_s). Thus, length changes demonstrate martensitic and bainitic transformation during the quenching and partitioning step. Samples were heated to 850 °C and then cooled slowly to 805 °C to develop ferritic grains by nucleation and growth. As described in Fig. 5, approximately 10% of untransformed austenite partially decomposed into ferritic at the second austenitization step, Fig. 7a. Fig. 7b shows the lattice expansion under quenching to 220 °C, indicating the 50% martensitic transformation of the prior austenite grains. Quenching aimed to transform half of the austenite from the intercritical treatment between Ac_1 and Ac_3. After quenching, the microstructure is composed of 10% ferrite, 45% martensite, and 45% austenite. Subsequently, the sample was heated to enhance carbon partitioning from saturated freshly formed martensite into the untransformed austenite phase.

Once the quenching had been carried out, two different temperatures were adopted to induce the partition of the alloying elements (mainly carbon) to the untransformed austenite in the quenching. Partition temperatures (isothermal heat treatment) were: 325 °C and 375 °C. Fig. 8 presents dilatometry data exclusively referring to the partition step for both chosen partition temperatures. It was possible to observe that despite an isothermal treatment (partition step) being applied, there was an expansion of the specimen, which is related to the decomposition of austenite at partition steps. This expansion during the partition step is probably correlated to the bainitic transformation of the remaining austenite.

After the partition step, the specimens were tempered at 400 °C to form tempered martensite, relieve the stresses related to the martensitic transformation, and enhance precipitate transition carbides inside the martensite laths without further phase transformation. Fig. 9 depicts the dilatometry tempering data for both heat treatments applied. Notice that there was no volumetric expansion or contraction during tempering, indicating the lack of evidence of austenite

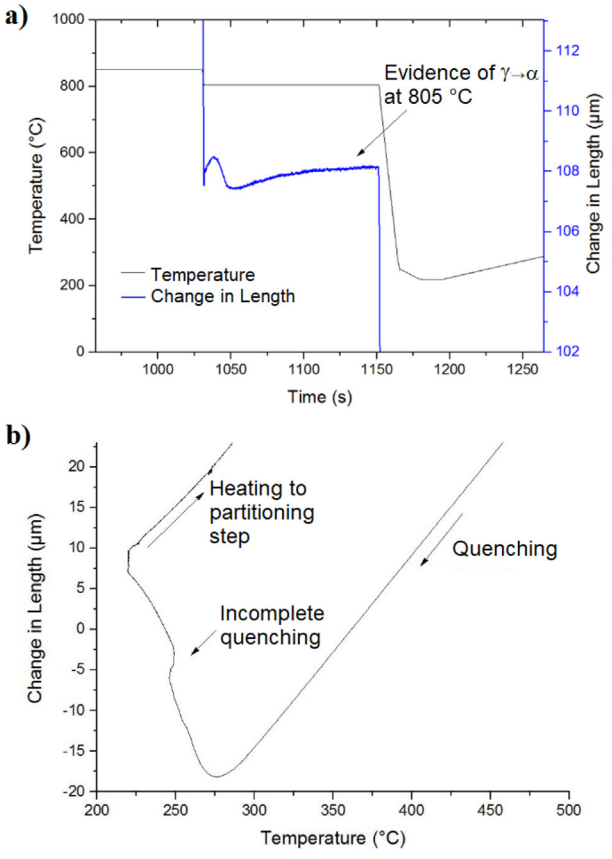

Fig. 7 – (a) Evidence of eutectoid transformation at 805 °C and (b) partial martensitic transformation at 220 °C after quenching.

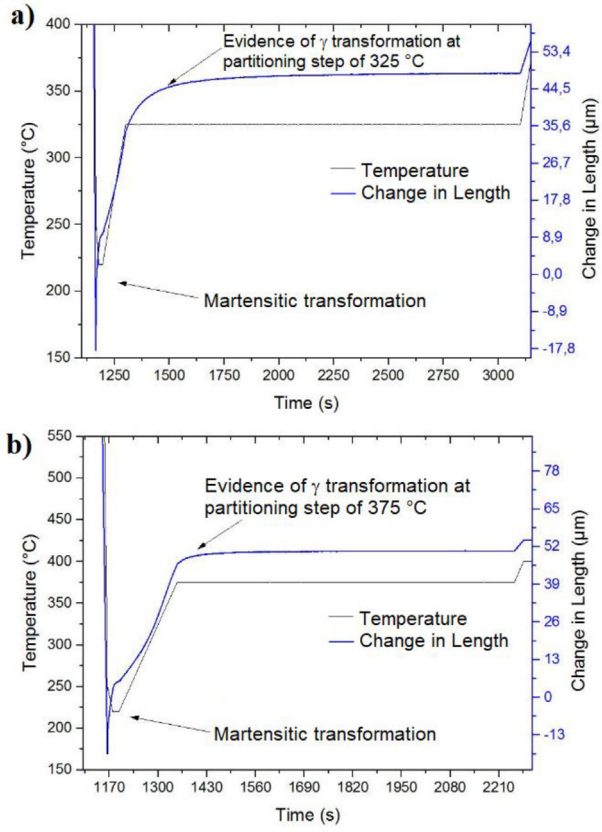

Fig. 8 – Evidence of austenite decomposition at (a) QP-220-325-400 and (b) QP-220-375-400 specimens. This expansion at the partition step is likely correlated to bainitic transformation.

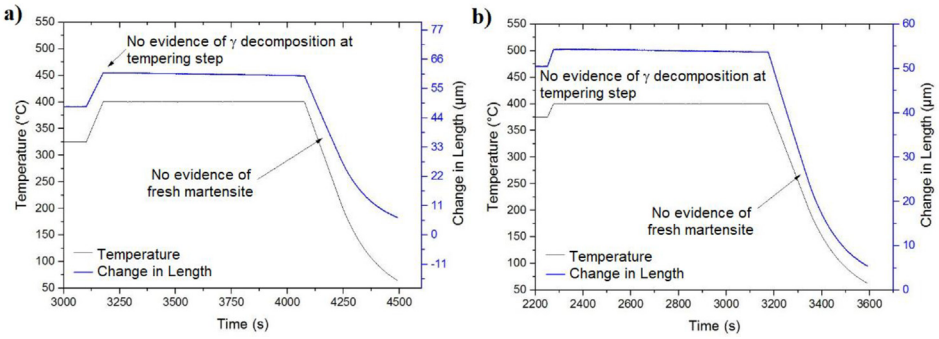

Fig. 9 – Tempering step for heat treatment of (a) QP-220-325-400 and (b) QP-220-375-400 partitioning temperatures.

decomposition due to the accuracy of dilatometry and low proportion of austenite fraction in this step. The specimens' smooth contraction without inflections is observed when cooling down to room temperature after tempering. Therefore, it is possible to imply that the final microstructure is absent from fresh martensite after each heat treatment. As a result of the thermal treatments, the microstructures composed of ferrite, martensite, a small fraction of bainite, and austenite stabilized at room temperature were observed.

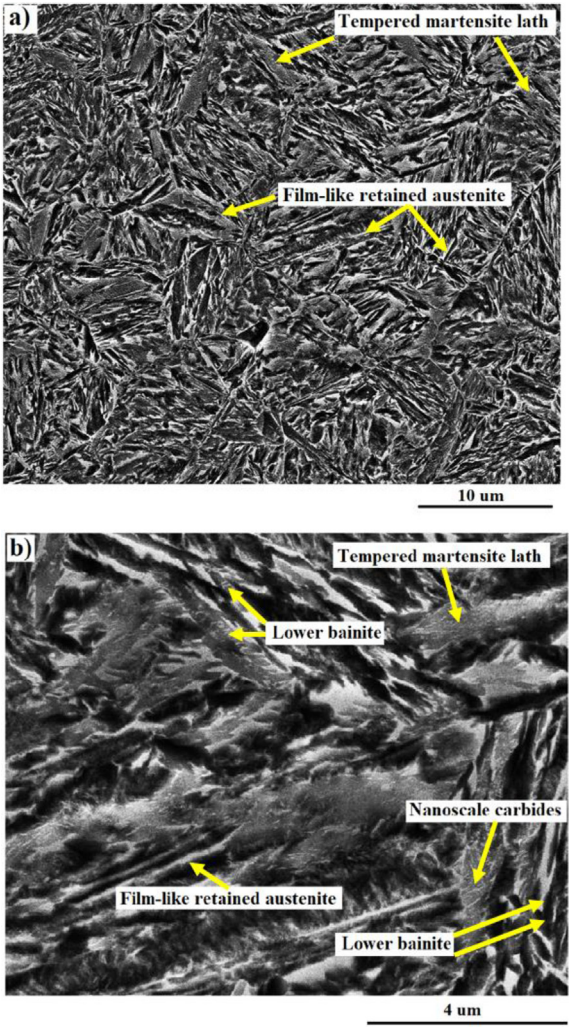

Fig. 10 – SEM micrographs of the QP-220-325-400 sample.

Fig. 10 shows the SEM micrographs of the QP-220-325-400-325 sample, mainly consisting of tempered martensite lath and bainitic sheaves coupled with film-like retained austenite at boundaries and nanoscale carbides within the bcc lath phases. It is expected that carbon is first partitioned from distorted primary martensite lath into adjacent untransformed austenite from martensite/austenite interfaces. Then, austenite partially decomposed into ferritic-bainite and carbide precipitations. The presence of nanoscale carbide precipitates with the martensite lath and bainitic sheaves indicate the austenite decomposition and carbon partitioning.

Fig. 11 shows the SEM micrographs of the QP-220-375-400 sample. In both conditions, a different amount of retained austenite and nanoscale carbide particles located between lath and plate-type of bcc tempered ferrite-martensite-bainite matrix boundary was formed. The volumetric fraction of each phase, their lattice parameters, and dislocation densities were estimated using the intensity-scattering vector plots to quantify the microstructure. It is shown that FCC γ-austenite and BCC α-ferrite were distinguished from the experimental crystallographic data. The variation in lattice strain of each phase provided evidence of possible austenite-to-martensite phase transformation during straining. The localized stress field could be concentrated on the initial yield stage where low, stable untransformed austenite is transformed into martensite at engineering strain below 6%. Results show that a significant deviation in yielding behavior will be noted in this stage due to the poor-Mn regions within the austenite phases. Therefore, Mn-rich baffles inside the retained austenite change the stacking fault energy (SFE) to promote twinning rather than martensitic transformation, especially after yielding [23]. The correlation between austenitic phase transformations on small tetragonality changes of the product martensite crystal lattice was conducted during selected heat treatments by analyzing the asymmetry of the BCC and FCC crystal orientations.

Although the study of microstructural evolution during Q&P coupled with bainitic transformation is restricted, EBSD measurements can characterize BCC-type ferritic structures containing ferrite/martensite/bainite morphology. Additionally, the volume fraction of meta-stable retained austenite dispersed in the microstructure can also be quantified. Fig. 12 shows the normal orientation image (OIM), ODF at constant $\varphi_2 = 45°$, and phase maps of both treated samples. Rapid quenching from the intercritical region into a temperature

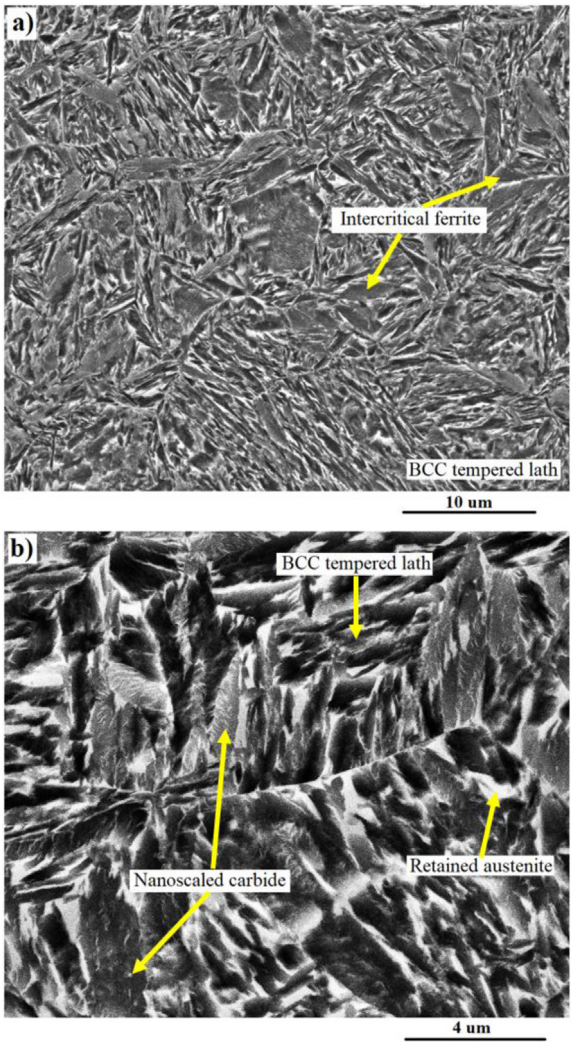

Fig. 11 – SEM micrographs of the QP-220-375-400 sample.

below martensite start transformation induced significant internal shear stress, resulting in a nanostructured lath-type martensite matrix. However, a semi-uniform nanoscale retained austenite dispersion was characterized. The volume fraction of this stable carbon-rich RA was estimated at approximately 8.5 ± 1.5% proportion on the QP-220-325-400 sample. This retained austenite at martensite inter-lath could improve fracture's toughness. Notably, a high mechanical resistance is guaranteed due to the development of tempered martensite microstructure. The partitioning step allows the rejection of excessive carbon from saturated martensite into neighbors inter-lath RA, leading to the tetragonality reduction and consequently a ductile macro performance. The thicker RA particles are present in the QP-220-375-400 (~12.5 ± 1.5%). The more refining BCC structure can be seen in the QP-220-325-400 sample due to the lower partitioning temperature. The excess shear strain generated higher lattice distortion and caused more boundaries. It is well-known that increasing the random or high-angle boundaries can effectively improve fracture toughness because they strongly hinder crack propagation. This study's multi-stage bainitic phase transformation also enhances the untransformed austenite decomposition into bainite components. It is probably that Si micro-segregation into austenite-ferrite interfaces prevents carbide formation; thereby, stable RA would result in the final microstructure [24]. Such stable RA could effectively improve the fracture toughness due to the TRIP effects. Meanwhile, bainitic transformation also increases the carbon-enrichment of untransformed RA because the bainite grows by diffusion mechanism.

Results revealed that ultrafine ferritic lath developed at lower partitioning temperature and nanostructure carbon-rich film-like retained austenite with a width less than 100 nm is stabled at ferritic lath. Interestingly, the soft RA surrounded by ferritic lath would be transformed into martensite at the final deformation stage, which would bring outstanding mechanical performance. The development of ultrafine ferritic lath is associated with forming many close-packed crystallographic orientations within each ferrite group. As it was previously explained, slipping occurs in the close-packed <111> direction in BCC structure, while {001}-planes have the least atomic density, making impossible crystallographic slippage. Therefore, grain fragmentation predominantly happens in these planes, confirmed by the orientation density functional orientation distribution function (ODF), shown in Fig. 12. Furthermore, the kinetics of diffusional carbon partitioning coupled with untransformed austenite decomposition into bainite also control the lath growth by neighboring austenite-ferrite interfaces [25–27]. Therefore, refined grains increase the hardenability due to the higher proportion of boundaries. Then, carbon atoms would move from distorted ferritic lattice into austenitic lattice atomic configuration, leading to strain gradient from boundaries toward the grain.

Lattice distortion segregation can alter the mechanical response. Lattice distortion crystallographic orientation changes can be classified in high-angle with point-to-point misorientation (θ) greater than 15° and low-angle boundaries with $5° < \theta < 15°$. Grain boundaries and ferritic lath with significant lattice distortion contain higher internal energy, acting as interstitial segregation favor sites. Atom probe tomography analyses could confirm these interstitial segregations.

Fig. 13 presents the misorientation angle distribution of both treated samples containing tempered martensite and bainite sheaves, as described in Figs. 10 and 11. It is shown that both BCC products have high misorientation angles significantly higher than 40°, resulting in high crystallographic defects (e.g., dislocation density). The BCC sheaves/carbide interface is the main barrier against dislocation moments and lattice sliding, increasing the mechanical resistance. Fig. 13 also exhibited that the lower temperature of the first partitioning step (325 °C) generated the more refined BCC sheaves due to the higher super-cooling, reducing the critical size for sheaves nucleation [28,29]. A high number of variants within the BCC sheaves shown in Fig. 12a and b is associated with the higher volumetric fraction of high misorientation angles in the resulting microstructure. De-Castro et al. [28] also reported greater stored energy in sheaves bainite/martensite structure with misorientation angles higher than 50° due to the broader crystallographic disorientation. Wang et al. [29] concluded that the bainite nucleus must possess a certain misorientation

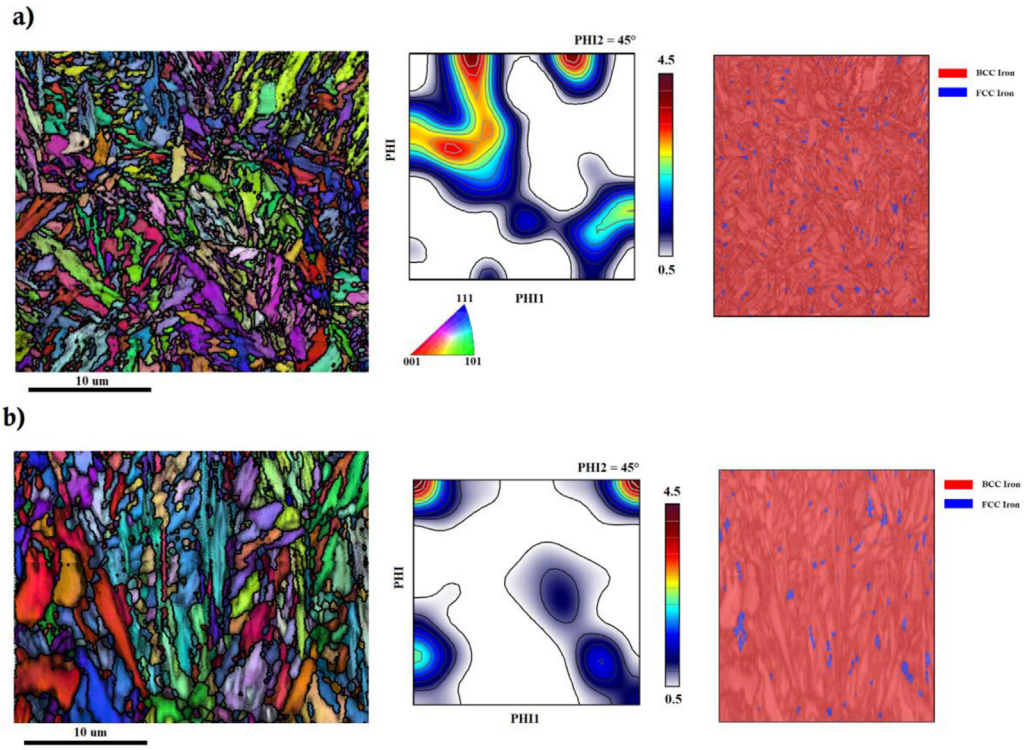

Fig. 12 – Normal direction orientation image (OIM), ODF at constant $\varphi_2 = 45°$, and phase maps of (a) QP-220-325-400 and (b) QP-220-375-400 samples.

angle to provide adequate activation energy to suppress the high α/γ interfacial energy. Therefore, the high angle grain boundaries, greater than 40°, could act as practical barriers to prompt and restrict transformation strain from penetrating the neighboring ferrite to accelerate bainitic transformation kinetics in the lamellar-structured specimen.

The produced intercritical ferrite/tempered martensite/nanostructure bainite BCC structure matrix in the presence of ~10% of nano-scaled (<100 nm) carbon-enriched retained austenite could demonstrate excellent properties to use in roller bearings, automotive industry, pipeline, and rail production. The nanometric width of retained austenite surrounded by ferritic lath, formed during the quenching then tempered in the partitioning stage, promotes the C–Mn–Si microsegregation at ferritic boundaries of ferrite-austenite interfaces. In addition, it is worth mentioning that the ultra-

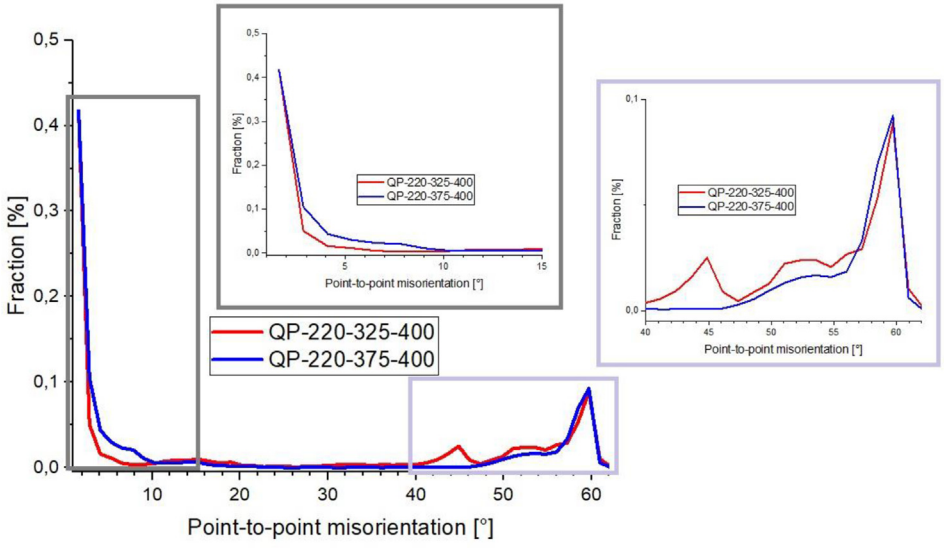

Fig. 13 – Distribution of point-to-point misorientation angle of both treated samples.

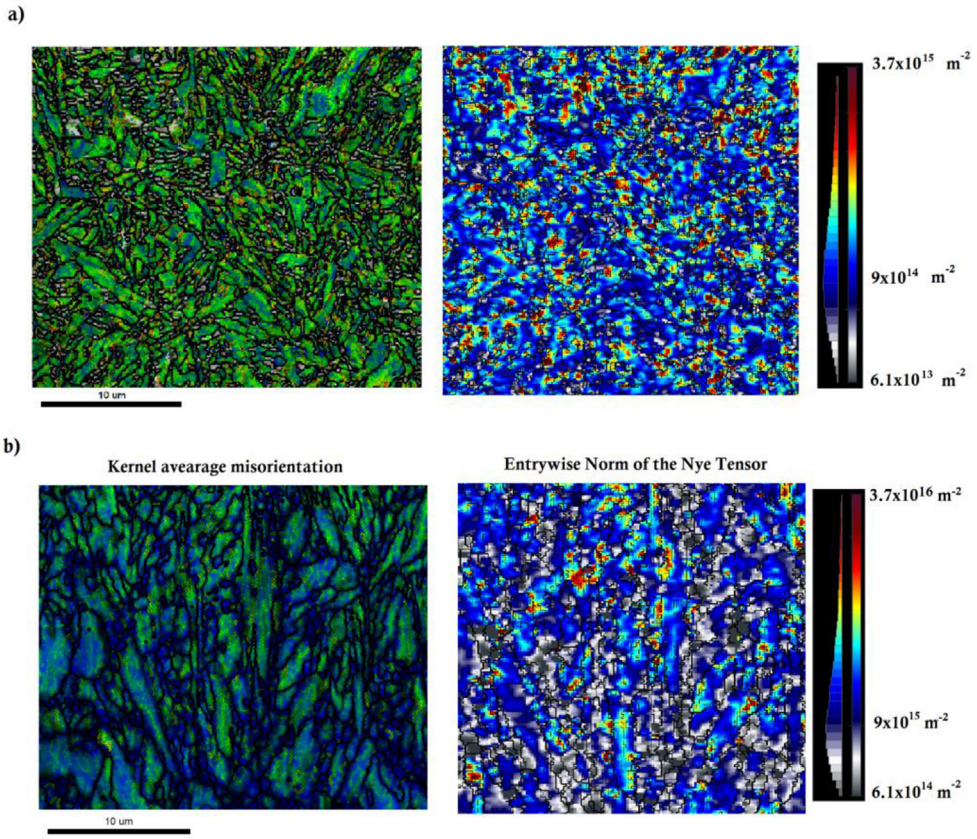

Fig. 14 – Kernel average misorientation (KAM) and geometrically necessary dislocation densities (GNDD) using Entrywise norm of the Nye tensor method for (a) QP-220-325-400 and (b) QP-220-375-400 samples.

fine carbides (<250 μm) disturb the dislocation movement in the ferritic matrix and can remarkably increase the mechanical resistance without decreasing the ductility [30,31].

The resulting micrographs exhibited that film-like and blocky type retained austenite were formed at the prior austenite grain boundaries and within the austenite grain, surrounded by BCC ferrite-bainite-martensite laths. Bainitic transformation can be compared with martensite transformation in restricted diffusion. The most accepted crystalline orientation relationships (OR) between the original FCC (γ) and produced BCC (α) is defined by Kurdjumov-Sachs (K–S), that there are 24 possible variants through the (111)γ||(011)α and [101]γ||[111]α orientations. In other words, closed-packed planes and directions in both atomic configurations are parallel.

Crystallographic data obtained by EBSD provides grain internal distortion detail analysis in terms of Kernel Average Misorientation (KAM) and Geometrically Necessary Dislocation Densities (GNDD), used to investigate and predict the activated deformation mechanism and crystal plasticity. In polycrystalline materials, the plastic deformation causes lattice distortion and forms boundaries, subgrain boundaries, dislocation cells, and pile-ups. KAM measures the distortion of each reference point with its nearest defined points. KAM is

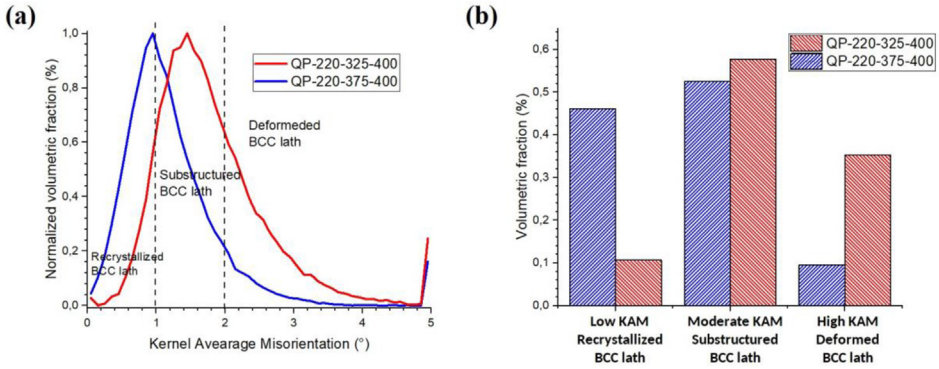

Fig. 15 – (a) Distribution of KAM values and (b) classification of BCC-sheaves products of both treated samples.

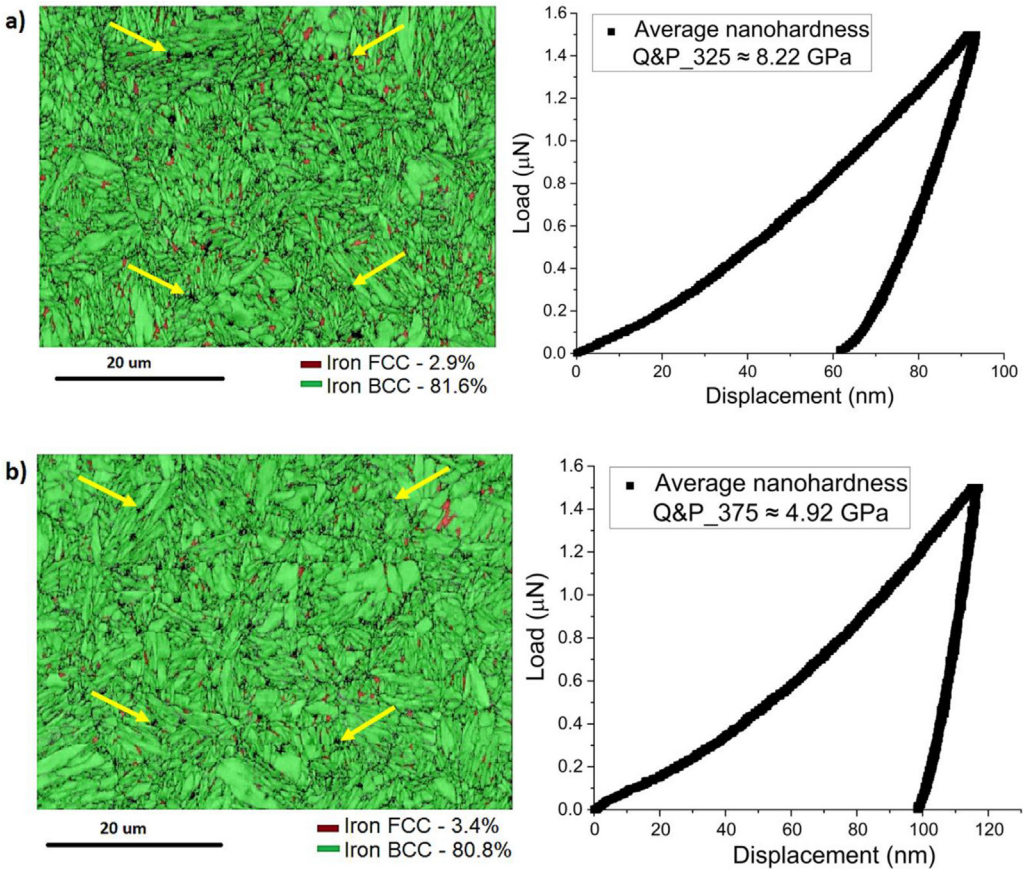

Fig. 16 – 10 × 10 mesh of the nanoindentations (black triangles, indicated by yellow arrows) superimposed on a phase identification map. The samples were quenched at 220 °C and Partitioned at: (a) 325 °C, (b) 375 °C. The green regions indicate the BCC (ferrite/martensite/bainite) phases, and the red regions of the FCC (austenite) phase.

evidence for lattice curvature and crystallographic defects to estimate local distortion. Local misorientations are governed by angular and spatial distortion, and a threshold angle in a range of 2°–5° can be set to avoid the interaction of any other crystal defects. The GNDD is associated with the lattice rotation gradient due to the dislocation arrangements [3] and can be calculated by the Nye-Kroner theory [3,32,33]. The lattice distortion map estimated using the Nye's tensor norm can present localized disorientation, as shown in Fig. 14.

The significant difference between BCC products such as ferrite, bainite, and martensite is the presence of a large amount of crystal distortion. Therefore, the use of KAM analyses could be a reliable method to determine the formation of each phase. For this purpose, a third nearest neighbor pixel was selected with a spatial resolution of approximately 300 nm with a threshold angle of 2°–5° to avoid obtaining high and meaningless KAM values at grain boundaries. Fig. 15a shows the distribution of KAM values. Quasi-strain-free low KAM values (KAM<1.0°) could be associated with the recrystallized BCC lath with no significant lattice distortion. While, by increasing the degree of lattice imperfection (such as dislocation densities), KAM values gradually increase. Fig. 14a and b show that the highest KAM values are mainly concentrated at sheaves interfaces, then gradually decreased towards the BCC lath/pocket products. Moderate KAM values (1°<KAM<2°) could be attributed to the substructured BCC lath due to the partial dislocation rearrangement to reduce internal energy by lattice distortion. However, high KAM values (KAM>2°) have a large amount of lattice imperfection containing higher stored energy, known as the primary site for possible micro-crack nucleation due to the higher lattice distortion and strain field accumulation.

The distortion noise calculated the disorientation and GNDD densities to estimate the spatial derivatives involving

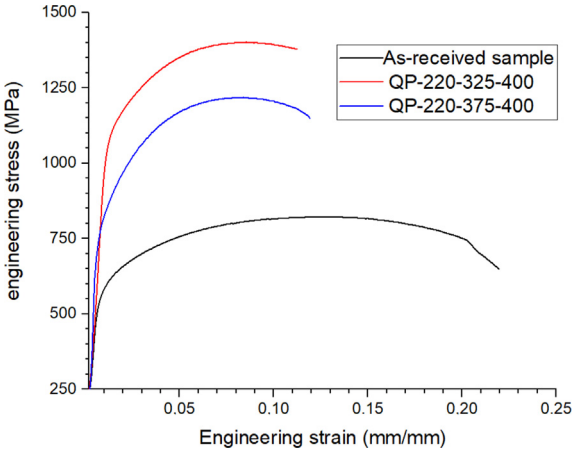

Fig. 17 – Engineering stress-strain curves obtained from subsized samples.

Table 2 – Tensile Data obtained from subsized curves of the investigated specimens.

Sample	Yield Stress [MPa]	Ultimate Tensile Strength [MPa]	Total elongation [%]	Toughness[a] [J/mm3]	Strain-Hardening Coefficient (n)[b]
As-received sample	495 ± 10	820 ± 15	0.21 ± 0.02	165.0 ± 5.0	0.145
QP-220-325-400	975 ± 25	1400 ± 25	0.12 ± 0.03	140.0 ± 5.0	0.161
QP-220-375-400	780 ± 25	1220 ± 25	0.13 ± 0.03	130.0 ± 5.0	0.188

[a] Toughness calculated from the area under the strain-stress curve.
[b] Strain-hardening coefficient calculated by the Hollomon equation.

orientation density functions and lattice curvatures. GNDD analysis revealed the dislocation cells, low-angle subgrains, and even high-angle boundaries. The latter boundaries vary from small to high disorientations to calculate average dislocation densities. The average dislocation densities in the Q&P-325 sample were estimated to be approximately 9×10^{14} m^{-2}, while the QP-220-375-400 sample showed 9×10^{15} m^{-2}, which means ten times higher. It would result in an extreme increase in mechanical resistance. Martensitic transformation under the quenching step induces high interfacial energy and increases the storing energy, causing the lath and plate martensite nuclei. Pure shear martensitic transformation along the dislocation slippage generates newly formed crystallographic defects dependent on the prior microstructure, which ferrite and austenite had been developed during the intercritical step. Then diffusional-aid bainitic transformation promoted carbon partitioning from saturated martensite into untransformed austenite. In this case, carbon-poor austenite regions decompose to carbide and ferritic-bainite. The role of Si in retard carbide precipitation is already known [34]; thereby, the more stable retained austenite was formed. It could have resulted from distorted martensite-austenite and martensite-ferrite interfaces, which can decrease the nucleation energy of martensite lath; then, a more refined structure can be formed in the QP-220-325-400 sample due to the lower temperatures. The combination of martensitic lath/plate martensite with bainite transformation coupled with carbon partitioning into untransformed austenite could be related to the localized stress field detected by the Nye's tensor norm maps. Since the localized stress produced by martensite transformation determines the coordinative plate slippage throughout adjacent grains, the small C atoms could be trapped and diffused through the lattice.

EBSD analysis and nanoindentation measurements were also correlated with the microconstituents and their characteristics. In Fig. 16, the results are presented for both Q&P samples quenched at 220 °C and partitioned at 325 °C and 325 °C for 30 min. The red regions correspond to the FCC austenitic phase, indicating this phase's size and distribution in the microstructure. The ferrite, bainite, and martensite (BCC or BCT structures) appear green. The results indicate nanohardness values of 8.22 ± 0.58 GPa and 4.92 ± 1.60 GPa for QP-220-325-400 and QP-220-375-400, respectively. The reduction in nanohardness could be attributed to the possible decrease in the density of dislocations, as previously discussed.

The engineering stress-strain data for the tensile tests of as-received commercial 9254 steel (proeutectoide ferrite + pearlite) and the heat-treated samples are presented in Fig. 17. The tensile properties such as yield stress (YS), ultimate tensile strength (UTS), total elongation (TE), toughness (area under the strain-stress curve), and strain-hardening coefficient (calculated by the Hollomon equation) are listed in Table 2. The lowest tensile resistance and highest total elongation are belonged to the as-received commercial sample due to the low cooling rate during production processing. While, complex proposed Q&P processing coupled with bainitic transformation developed martensite/bainite lath BCC matrix with nanostructured carbide dispersion, resulting in a considerable increase in the mechanical resistance. For instance, the ultimate tensile strength increased about 70% and 48% in QP-220-325-400 and QP-220-375-400 samples, respectively.

On the other hand, the ductility of commercial samples is reduced by dispersive phase transformation. Therefore, total elongation before fracture was reduced by about 43% and 38% of QP-220-325-400 and QP-220-375-400 samples, respectively. It is well-known that brittle fracture suddenly occurs without any noticeable elongation, in the absence of any necking of the specimens, defined by a fracture strain of less than 5%. Therefore, the ductility of 12 and 13% obtained in the studied steel after heat treatments could be acceptable in many industrial applications, considering an excellent increasing the tensile resistance (~1400 MPa). Moreover, the toughness, defined as the ability of the structure to absorb energy before failure, was calculated from the area under the stress-strain curve, known as the modulus of toughness, and exhibited a subtle reduction (~18 ± 3% MPa/mm/mm) in the treated samples compared to as-received commercial ones. Therefore, applying the proposed heat treatments can successfully reduce wall/plate thickness with a reduced loss of ductility and toughness.

4. Conclusions

The present study reveals the significant influence of transformations temperature on the fraction of microconstituents in Q&P treatments. Furthermore, Austenite decomposition in the complex phase steel consisting of ferrite, bainite, and martensite was observed by scanning electron microscopy and confirmed the predictions aiming for a tailored complex multicomponent microstructure development.

The intercritical treatment between Ac1 and Ac3 induces the formation of controlled ferrite fractions. As a consequence of this decomposition, the remaining austenite enriches to induce the formation of carbon-rich martensite. Although carbon atoms were partitioning from saturated martensite during the partitioning step, untransformed austenite

decomposed into transition nanoscale carbide particles and ferritic-bainite structure. Bainitic transformation formed the carbon-enriched film-like retained austenite at boundaries and nanocarbides particles within the bcc laths.

On the one hand, the development of refined martensite-bainitic structures with high stored energy would result in high mechanical resistance. On the other hand, the nanoscale carbide acts as a barrier against dislocation movements, and the surrounded film-like retained austenite increases the fracture toughness by the TRIP effect. Such complex multi-component lath-type structures obtained by designed Q&P heat treatment on commercial carbon-silicon spring steel showed localized mechanical resistance varying from 4.92 GPa for the QP-220-375-400 to 8.22 GPa for the QP-220-325-400 samples determined by nanoindentation test. In addition, high ultimate tensile and yield strength, up to 1400 MPa and 975 MPa, were achieved in the QP-220-375-400 sample due to a set of complex multicomponent lath-type nanostructures designed by Q&P coupled with bainitic transformation, with good fracture strain (~0.12%).

Declaration of Competing Interest

The authors declare that they have no known competing financial interests or personal relationships that could have appeared to influence the work reported in this paper.

Acknowledgments

The authors acknowledge the financial support provided by the National Council of Scientific and Technological Development - CNPq (grant number 304157/2020–1 and 309160/2016–2) and São Paulo Research Foundation – FAPESP (grant number 2021/02926–4). Julian A. Avila is a Serra Hunter Fellow.

REFERENCES

[1] Speer J, Matlock DK, De Cooman BC, Schroth JG. Carbon partitioning into austenite after martensite transformation. Acta Mater 2003;51:2611–22. https://doi.org/10.1016/S1359-6454(03)00059-4.

[2] Speer JG, De Moor E, Clarke AJ. Critical assessment 7: quenching and partitioning. Mater Sci Technol 2015;31:3–9. https://doi.org/10.1179/1743284714Y.0000000628.

[3] Ernould C, Beausir B, Fundenberger JJ, Taupin V, Bouzy E. Global DIC approach guided by a cross-correlation based initial guess for HR-EBSD and on-axis HR-TKD. Acta Mater 2020;191:131–48. https://doi.org/10.1016/j.actamat.2020.03.026.

[4] Ariza EA, Masoumi M, Tschiptschin AP. Improvement of tensile mechanical properties in a TRIP-assisted steel by controlling of crystallographic orientation via HSQ&P processes. Mater Sci Eng 2018;713:223–33. https://doi.org/10.1016/j.msea.2017.12.046.

[5] Xiong XC, Chen B, Huang MX, Wang JF, Wang L. The effect of morphology on the stability of retained austenite in a quenched and partitioned steel. Scr Mater 2013;68:321–4. https://doi.org/10.1016/j.scriptamat.2012.11.003.

[6] Ariza EA, Nishikawa AS, Goldenstein H, Tschiptschin AP. Characterization and methodology for calculating the mechanical properties of a TRIP-steel submitted to hot stamping and quenching and partitioning (Q&P). Mater Sci Eng 2016;671:54–69. https://doi.org/10.1016/j.msea.2016.06.038.

[7] Nishikawa AS, Santofimia MJ, Sietsma J, Goldenstein H. Influence of bainite reaction on the kinetics of carbon redistribution during the quenching and partitioning process. Acta Mater 2018;142:142–51. https://doi.org/10.1016/j.actamat.2017.09.048.

[8] Celada-Casero C, Kwakernaak C, Sietsma J, Santofimia MJ. The influence of the austenite grain size on the microstructural development during quenching and partitioning processing of a low-carbon steel. Mater Des 2019;178. https://doi.org/10.1016/j.matdes.2019.107847.

[9] Celada-Casero C, Sietsma J, Santofimia MJ. The role of the austenite grain size in the martensitic transformation in low carbon steels. Mater Des 2019;167. https://doi.org/10.1016/j.matdes.2019.107625.

[10] Bigg TD, Edmonds DV, Eardley ES. Real-time structural analysis of quenching and partitioning (Q&P) in an experimental martensitic steel. J Alloys Compd 2013;577:S695–8. https://doi.org/10.1016/j.jallcom.2013.01.205.

[11] Clarke AJ, Speer JG, Miller MK, Hackenberg RE, Edmonds DV, Matlock DK, et al. Carbon partitioning to austenite from martensite or bainite during the quench and partition (Q&P) process: a critical assessment. Acta Mater 2008;56:16–22. https://doi.org/10.1016/j.actamat.2007.08.051.

[12] Echeverri EAA, Nishikawa AS, Masoumi M, Pereira HB, Marulanda NG, Rossy AM, et al. In situ synchrotron X-ray diffraction and microstructural studies on cold and hot stamping combined with quenching & partitioning processing for development of third-generation advanced high strength steels. Metals 2022;12:174. https://doi.org/10.3390/met12020174.

[13] Masoumi M, Echeverri EAA, Tschiptschin AP, Goldenstein H. Improvement of wear resistance in a pearlitic rail steel via quenching and partitioning processing. Sci Rep 2019;9:7454. https://doi.org/10.1038/s41598-019-43623-7.

[14] Ernould C, Beausir B, Fundenberger JJ, Taupin V, Bouzy E. Integrated correction of optical distortions for global HR-EBSD techniques. Ultramicroscopy 2021;221. https://doi.org/10.1016/j.ultramic.2020.113158.

[15] Oliver WC, Pharr GM. An improved technique for determining hardness and elastic modulus using load and displacement sensing indentation experiment. Mater Res Soc 1992;7:1564–78.

[16] Yan X, Liaw PK, Zhang Y. Ultrastrong and ductile BCC high-entropy alloys with low-density via dislocation regulation and nanoprecipitates. J Mater Sci Technol 2022;110:109–16. https://doi.org/10.1016/j.jmst.2021.08.034.

[17] Wang J, Kou Z, Fu S, Wu S, Liu S, Yan M, et al. Ultrahard BCC-AlCoCrFeNi bulk nanocrystalline high-entropy alloy formed by nanoscale diffusion-induced phase transition. J Mater Sci Technol 2022;115:29–39. https://doi.org/10.1016/j.jmst.2021.11.025.

[18] Sabet Ghorabaei A, Nili-Ahmadabadi M. Effects of prior austenite grain size and phase transformation temperature on bainitic ferrite formation in multi-constituent microstructures of a strong ultra-low-carbon steel. Mater Sci Eng 2021;815:141300. https://doi.org/10.1016/j.msea.2021.141300.

[19] Peng F, Xu Y, Han D, Gu X. Kinetic models of multiple-stage martensite transformation and subsequent isothermal bainite formation excluding ε-carbide precipitation in intercritical quenching and partitioning steels. Mater Des 2019;183:108183. https://doi.org/10.1016/j.matdes.2019.108183.

[20] Peng F, Xu Y, Li J, Gu X, Wang X. Interaction of martensite and bainite transformations and its dependence on quenching temperature in intercritical quenching and partitioning steels. Mater Des 2019;181:107921. https://doi.org/10.1016/j.matdes.2019.107921.
[21] Luiggi A NJ. Study of elastic, structural, electronic, magnetic, and topological properties of η-Fe 2 C carbide under pressure. J Phys Chem Solid 2019;131:196–212. https://doi.org/10.1016/j.jpcs.2019.03.032.
[22] Wei H, li Chen Y, Yu W, Su L, Wang X, Tang D. Study on corrosion resistance of high-strength medium-carbon spring steel and its hydrogen-induced delayed fracture. Constr Build Mater 2020;239:117815. https://doi.org/10.1016/j.conbuildmat.2019.117815.
[23] Shen YF, Dong XX, Song XT, Jia N. Carbon content-tuned martensite transformation in low-alloy TRIP steels. Sci Rep 2019;9:1–9. https://doi.org/10.1038/s41598-019-44105-6.
[24] Zhang L, Radiguet B, Todeschini P, Domain C, Shen Y, Pareige P. Investigation of solute segregation behavior using a correlative EBSD/TKD/APT methodology in a 16MND5 weld. J Nucl Mater 2019;523:434–43. https://doi.org/10.1016/j.jnucmat.2019.06.002.
[25] Haghdadi N, Cizek P, Hodgson PD, Tari V, Rohrer GS, Beladi H. Effect of ferrite-to-austenite phase transformation path on the interface crystallographic character distributions in a duplex stainless steel. Acta Mater 2018;145:196–209. https://doi.org/10.1016/j.actamat.2017.11.057.
[26] Zhao H, Palmiere EJ. Effect of austenite grain size on acicular ferrite transformation in a HSLA steel. Mater Char 2018;145:479–89. https://doi.org/10.1016/j.matchar.2018.09.013.
[27] Masoumi M, Silva CC, Béreš M, Ladino DH, de Abreu HFG. Role of crystallographic texture on the improvement of hydrogen-induced crack resistance in API 5L X70 pipeline steel. Int J Hydrog Energy 2017;42:1318–26. https://doi.org/10.1016/j.ijhydene.2016.10.124.
[28] De-Castro D, Eres-Castellanos A, Vivas J, Caballero FG, San-Martín D, Capdevila C. Morphological and crystallographic features of granular and lath-like bainite in a low carbon microalloyed steel. Mater Char 2022;184:111703. https://doi.org/10.1016/j.matchar.2021.111703.
[29] Wang T, Qian L, Yu W, Li K, Zhang F, Meng J. Effect of ferrite-austenite morphology and orientation relationship on bainite transformation in low-alloy TRIP steels. Mater Char 2022;184:111656. https://doi.org/10.1016/j.matchar.2021.111656.
[30] Cong J, Li J, Fan J, Misra RDK, Xu X, Wang X. Effect of austenitic state before ferrite transformation on the mechanical behavior at an elevated temperature for seismic-resistant and fire-resistant constructional steel. J Mater Res Technol 2021;13:1220–9. https://doi.org/10.1016/j.jmrt.2021.05.061.
[31] Lo KH, Shek CH, Lai JKL. Recent developments in stainless steels. Mater Sci Eng R Rep 2009;65:39–104. https://doi.org/10.1016/j.mser.2009.03.001.
[32] Kysar JW, Saito Y, Oztop MS, Lee D, Huh WT. Experimental lower bounds on geometrically necessary dislocation density. Int J Plast 2010;26:1097–123. https://doi.org/10.1016/j.ijplas.2010.03.009.
[33] El-Dasher BS, Adams BL, Rollett AD. Viewpoint: experimental recovery of geometrically necessary dislocation density in polycrystals. Scr Mater 2003;48:141–5. https://doi.org/10.1016/S1359-6462(02)00340-8.
[34] Miettunen I, Ghosh S, Somani MC, Pallaspuro S, Kömi J. Competitive mechanisms occurring during quenching and partitioning of three silicon variants of 0.4 wt.% carbon steels. J Mater Res Technol 2021;11:1045–60. https://doi.org/10.1016/j.jmrt.2021.01.085.